



# Model-Based Parametric Study of Surface-Breaking Defect Characterization Using Half-Skip Total Focusing Method

Xiangyu Lei<sup>1</sup> · Håkan Wirdelius<sup>2</sup> · Johan E. Carlson<sup>3</sup>

Received: 10 November 2022 / Accepted: 27 March 2023  
© The Author(s) 2023

## Abstract

As the demand of structural integrity in manufacturing industries is increasing, the ultrasonic array technique has drawn more attention thanks to its inspection flexibility and versatility. By taking advantage of the possibility of individual triggering of each array element, full matrix capture (FMC) data acquisition strategy has been developed that contains the entire information of an inspection scenario. Total focusing method (TFM) as one of the ultrasonic imaging algorithms, is preferably applied to FMC dataset since it uses all information in FMC to synthetically focus the sound energy at every image pixel in the region of interest. Half-skip TFM (HSTFM) is proposed in multi-mode TFM imaging that involves a backwall reflection wave path, so that the defect profile could be reconstructed for accurate defect characterization. In this paper, a method involving Snell's law-based wave mode conversion is proposed to account for more reasonable wave propagation time when wave mode conversion happens at backwall reflection in HSTFM. A series of model based simulations (in software simSUNDT) are performed for parametric studies, with the intention of investigating the capability of defect characterization using HSTFM with varying tilt angle and relative position of surface-breaking notch to array probe. The results show that certain TFM modes could help with defect characterization, but the effectiveness is limited with varying defect features. It is inappropriate to address a certain mode for all characterization perspectives but rather a combination, i.e., multi-mode TFM, should be adopted for possible interpretation and characterization of defect features.

**Keywords** Ultrasonic array · Defect characterization · Total focusing method · Simulation · simSUNDT

## 1 Introduction

Testing methods are playing an important role with the increasing demand of structural integrity and quality assurance in manufacturing processes, especially in safety prioritized industries such as aerospace industry. Nondestructive

evaluation (NDE) and its testing methods have been proven promising in this context and are widely applied in related studies [1–3]. Ultrasonic phased array (PA) technique as one of the nondestructive testing (NDT) methods, has drawn more attention comparing to conventional ultrasonic testing (UT) method thanks to its improved inspection speed, flexibility and sensitivity [4, 5, 6]. The ultrasonic PA probe is made up of a series of piezoelectric crystal elements that can be triggered individually [7], so that various sound beam patterns such as beam steering and focusing [8], can be emulated by simply adjusting the circuit timing, i.e., delay law. A data acquisition strategy called full matrix capture (FMC) that takes advantage of the individual triggering feature of ultrasonic PA probe has also been developed [9]. The main idea of this strategy is to trigger one piezoelectric element (transmitter) of the PA probe at a time and record signal responses on all elements (receivers), then the next element is triggered to record another set of signal responses on all elements, and so on. In this way, all elements are triggered in sequence to record corresponding signal responses from all elements, so

---

✉ Xiangyu Lei  
leixiangyu1992@outlook.com

Håkan Wirdelius  
hakan.wirdelius@hv.se

Johan E. Carlson  
johan.carlson@ltu.se

<sup>1</sup> Department of Industrial and Materials Science (IMS), Chalmers University of Technology, 41296 Gothenburg, Sweden

<sup>2</sup> Division of Subtractive and Additive Manufacturing, University West, 46186 Trollhättan, Sweden

<sup>3</sup> Division of Signals and Systems, Luleå University of Technology, 97187 Luleå, Sweden

that a PA probe with  $N$  elements will have  $N$  by  $N$  signal responses in total as its FMC dataset.

By recording inspection signals from all available transmitter–receiver pairs of a PA probe, the FMC dataset contains complete information of an inspection scenario, which facilitates different beam forming operations and imaging processes during post-processing [9]. There are a number of imaging algorithms available using FMC dataset, such as inverse wave field extrapolation [10], wavenumber algorithm [11], synthetic aperture focusing technique (SAFT) [12] and total focusing method (TFM) [9]. The TFM algorithm synthetically focuses the wave energy at every image pixel, so that high image intensity could be revealed if the pixel is associated with a scatterer [13].

Depending on the prescribed ultrasound wave path in test specimen for reconstructing TFM images, the TFM algorithm can generally be characterized into three modes, i.e., direct path, half-skip path and full-skip path mode [14]. The direct path mode indicates that the wave has no reflection on backwall, while half-skip path includes backwall reflection at either transmission or reception and full-skip path contains backwall reflection at both transmission and reception of sound wave. These modes can generate different TFM images and could be useful for defect characterization depending on the defect features. This means that not all modes give clear indication of defect features [15]. Thus, care must be taken when choosing the appropriate TFM modes and images for defect characterization. It is beneficial to combine these modes for a thorough analysis of a defect in question, i.e., multi-mode TFM analysis [14–17].

Traditionally all qualification methodologies have been empirically based on extensive experimental works with test pieces. An infinite number of variables and possibilities then must be reduced into a limited group of statistically relevant NDT situations. Even though the proposed qualification procedure with test pieces is expensive, it also tends to introduce misalignments between the actual NDT situation that is to be performed and the proposed experimental simulation. Besides the problem of reconstructing the geometry and material, the fabricated defects must also be introduced with a verified prescription of their sizes and NDT characteristics. Service induced cracks (e.g., fatigue cracks and stress corrosion cracks) are to significant extent introduced in the inner surface of e.g., pipes and include tip diffraction phenomena into the interaction with ultrasonic energy, which tends to be difficult to reproduce in artificially manufactured defects. For a surface-breaking notch, half-skip TFM (HSTFM) can be applied to image the notch profile as it accounts reflections of waves on notch surface. This enables defect sizing using e.g., 6 dB drop rule based on the HSTFM images, instead of measuring the distance between indications of top and root diffraction in direct path TFM images [18, 19].

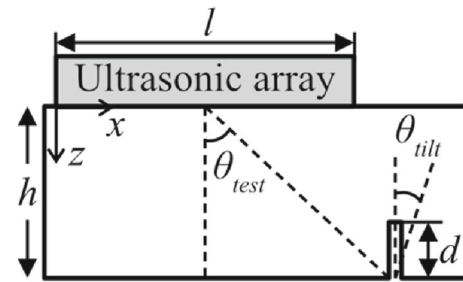


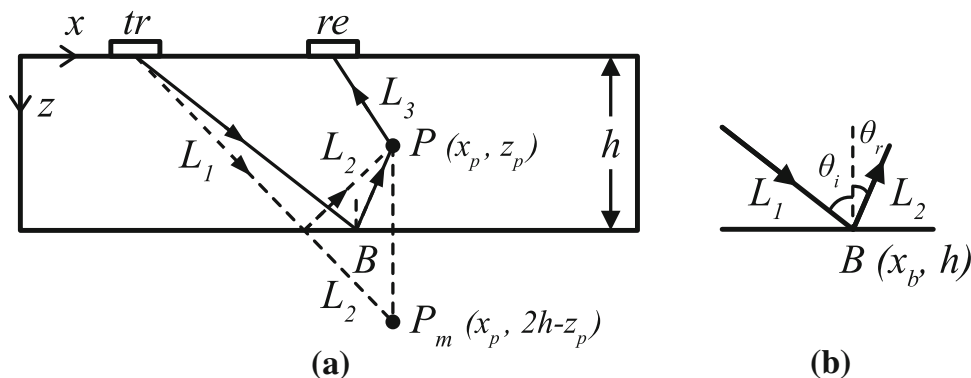
Fig. 1 The general inspection scenario considered in this paper

In this paper, further explorations are conducted on HSTFM algorithm when wave mode conversion happens at reflection on specimen backwall, which get Snell's law involved. This is to account for more accurate calculation of time-of-flight (TOF) of sound wave in TFM. Then this new HSTFM algorithm is applied to an experimental FMC dataset and a series of simulated FMC datasets (by software simSUNDT) for parametric studies, with the intention of investigating the capability of defect characterization using HSTFM when defect features are varying, such as tilt angle and the relative position of defect to PA probe. This again intends to reveal the sensitivity of TFM modes and images to defect features, and to give a potential guide for appropriate choices. When it comes to the relative position of defect to PA probe, some approaches regarding removal of backwall reflection signals are reviewed and discussed, aiming at eliminating the influence of backwall reflection signals in defect characterization. The effects of these approaches are evaluated and compared with simulated signals from simSUNDT, which is able to entirely suppress the backwall reflection signals.

## 2 General Inspection Scenario and Setup

The studies and collected FMC datasets in this paper are all based on a general inspection scenario and setup shown in Fig. 1. The data acquisition hardware unit TOPAZ64 from ZETEC company is a 64-channel phased array ultrasonic testing equipment. The PA probe used in the experiments with notation of LM-5MHz from ZETEC is a 64-crystal linear phased array longitudinal-wave probe with nominal center frequency of 5 MHz and bandwidth of 74%. The ultrasonic array (linear PA probe) is placed on top surface of a stainless steel test specimen with height ( $h$ ) of 35 mm, longitudinal and transverse wave speed of 5573 m/s and 3150 m/s, respectively. The origin of coordinate system is placed at the bottom-left end of the PA probe. A surface-breaking electric discharge machined (EDM) notch is located at specimen backwall with size ( $d$ ) of 5 mm. The linear PA probe used in the studies has 64 elements (labelled as LM-5MHz from

**Fig. 2 a** The wave path considered in conventional HSTFM (dashed line) and in HSTFM with Snell’s law-based wave mode conversion involved (solid line). **b** Local illustration of wave reflection in Snell’s law



Zetec) with nominal center frequency of 5 MHz and bandwidth of 74%. With each element of 0.5 mm in length and kerf of 0.1 mm in x-direction, the effective length (*l*) is 38.3 mm. The other dimension (out of plane) of the elements are 10 mm. The relative position between the probe center and notch root is expressed by  $\theta_{rest}$  and the positive tilt angle of the notch  $\theta_{tilt}$  is defined in clockwise direction. It is noted that the experimental test specimen used in this paper has only  $\theta_{tilt} = 0^\circ$ .

### 3 Snell’s Law-Based Wave Mode Conversion in HSTFM

When calculating the distance-of-flight (DOF) of ultrasonic waves in HSTFM, see Fig. 2a, the wave path length from transmitter (*tr*) to the current image pixel *P* with coordinate ( $x_p, z_p$ ), is calculated by connecting a straight line (dashed line) between transmitter and a mirrored pixel of *P* over the specimen backwall, i.e.,  $P_m$  with coordinate ( $x_p, 2h - z_p$ ). The transmitting part of wave path length  $L_{tr} = L_1 + L_2$  can then be calculated by Eq. (1) and the receiving part  $L_3$  is calculated by Eq. (2), where  $x_{tr}$  and  $x_{re}$  are the x-coordinate of transmitter and receiver, respectively.

$$L_{tr} = L_1 + L_2 = \sqrt{(x_p - x_{tr})^2 + (2h - z_p)^2} \tag{1}$$

$$L_3 = \sqrt{(x_p - x_{re})^2 + z_p^2} \tag{2}$$

The individual wave path length of  $L_1$  and  $L_2$  can also be retrieved according to the principle of similar triangle, expressed in Eq. (3).

$$L_1 = \frac{h \times L_{tr}}{2h - z_p}, L_2 = \frac{(h - z_p) \times L_{tr}}{2h - z_p} \tag{3}$$

Wave mode (either longitudinal or transverse) conversion is thereby included in HSTFM by assigning the corresponding wave speed to each wave path of  $L_1$  and  $L_2$  to calculate

the total TOF of sound wave. This approach of accounting wave mode conversion in HSTFM is referred as conventional HSTFM in this paper, whose accuracy is limited, because the Snell’s law [20] is not considered when the transmitting wave reflects at specimen backwall if wave mode converts. According to Snell’s law shown in Fig. 2b, the incident wave angle  $\theta_i$  should differ from reflected wave angle  $\theta_r$  if there is wave mode conversion at the reflection point *B* with coordinate ( $x_b, h$ ), following Eq. (4), where  $c_i$  and  $c_r$  are corresponding wave speeds for incident and reflected wave, respectively.

$$\frac{\sin\theta_i}{c_i} = \frac{\sin\theta_r}{c_r} \tag{4}$$

To account for the transmitting part of wave path length  $L_{tr}$  based on Snell’s law in Eq. (4), the position of reflection point *B*, i.e., coordinate  $x_b$  is therefore essential. To find this coordinate, Eq. (4) is rewritten as a function  $f(x_b)$  in Eq. (5).

$$f(x_b) = \frac{\sin\theta_i}{c_i} - \frac{\sin\theta_r}{c_r} = \frac{x_b - x_{tr}}{c_i \sqrt{(x_b - x_{tr})^2 + h^2}} - \frac{x_p - x_b}{c_r \sqrt{(x_p - x_b)^2 + (h - z_p)^2}} \tag{5}$$

The unknown coordinate  $x_b$  can be found by setting  $f(x_b) = 0$  so that the Snell’s law is satisfied. The individual wave path length of  $L_1$  and  $L_2$  can therefore be obtained through Eqs. (6) and (7). The remaining TOF calculation should be the same as earlier.

$$L_1 = \frac{x_b - x_{tr}}{\sin(\theta_i)} = \frac{x_b - x_{tr}}{\sin(\tan^{-1}(\frac{x_b - x_{tr}}{h}))} \tag{6}$$

$$L_2 = \frac{x_p - x_b}{\sin(\theta_r)} = \frac{x_p - x_b}{\sin(\tan^{-1}(\frac{x_p - x_b}{h - z_p}))} \tag{7}$$

As an illustration of the effect with and without involving Snell’s law at backwall reflection, HSTFM images in wave mode sequence of LTT (in sequence of  $L_1$ - $L_2$ - $L_3$  according to Fig. 2a, “L” for longitudinal wave and “T” for transverse

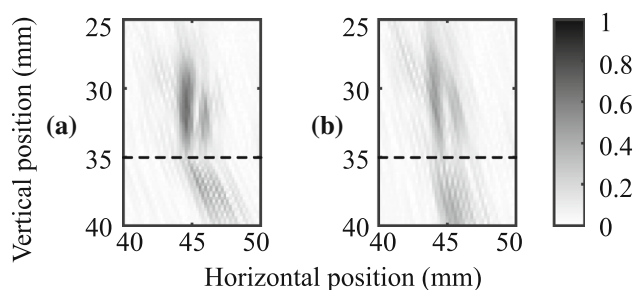


**Fig. 3** **a** Reconstructed HSTFM image with Snell's law involved and **b** not involved at backwall reflection in wave mode sequence of LTT for inspection scenario in Sect. 2 with  $\theta_{test} \approx 36^\circ$  based on experimental FMC dataset with  $\theta_{ilt} = 0^\circ$ . The dashed line indicates the position of the specimen backwall at 35 mm depth

wave) are reconstructed in Fig. 3 for an experimental FMC dataset under the inspection scenario introduced in Sect. 2 where  $\theta_{test} \approx 36^\circ$  and  $\theta_{ilt} = 0^\circ$  in Fig. 1. The dashed line indicates the position of the specimen backwall at 35 mm depth. The difference in notch tilt angle indications is obvious and it would mislead the interpretation of the defect feature if the Snell's law-based wave mode conversion is excluded in Fig. 3b. Thus, Snell's law-based wave mode conversion will be involved in all upcoming studies and HSTFM images in this paper.

#### 4 Subtraction of backwall reflection signals

Consider an inspection scenario in Fig. 1 with  $\theta_{test} \approx 0^\circ$ , i.e., the probe projection area completely covers the notch. In this case, the existence of strong backwall reflection would introduce extensive image artifacts in HSTFM images with certain wave mode sequence, e.g., if all wave paths are in longitudinal wave mode (LLL) [18]. As a result, the possible notch indication could be entirely covered by this image artifacts under the probe area, which hinders the defect detection and possible characterization.

An idea called FMC subtraction was brought up for suppressing the backwall reflection signals [21]. It is based on the phenomenon that for the transmitter–receiver pairs of the same lateral separation, the wave path lengths of backwall reflection are the same for a parallel sided test specimen, but different for the wave path lengths of a defect. Thus, it is assumed that the backwall reflection signals will have the same arrival time and amplitude, while these are different for defect signals. Based on this assumption, the backwall reflection signal for element pair  $(i, j)$ , i.e., the  $i$ th transmitter and  $j$ th receiver, can be extracted through summing and averaging signals from all element pairs with the same lateral separation, i.e.,  $|i - j|$ . The processed signal of element pair  $(i, j)$  with backwall reflection suppressed,  $S(i, j)$ , can be expressed by subtracting the extracted backwall reflection

signal from the original one,  $I(i, j)$ , as in Eq. (8).

$$S(i, j) = I(i, j) - \frac{1}{2(N - |i - j|)} \times \sum_{k=1}^{N-|i-j|} (I(k, k + |i - j|) + I(k + |i - j|, k)) \quad (8)$$

An example of this FMC subtraction result is shown in Fig. 4a for the pair tr1-re1 (the first element as both transmitter and receiver) from inspection case in Fig. 1 with  $\theta_{test} \approx 0^\circ$  and  $\theta_{ilt} = 0^\circ$ . The normalized raw signal (thin solid line) of FMC dataset is experimentally collected and the first backwall reflection appears at approximately  $12.5 \mu s$  and the second at approximately  $25 \mu s$ . It is clear from the local illustration box in Fig. 4a that the backwall reflection signal (dot dashed line) is successfully extracted from all element pairs with no separation in this example (same element as transmitter and receiver). However, the processed signal after FMC subtraction (thick solid line) using Eq. (8) still preserves backwall reflection signal within this time region, which has higher amplitude than a possible defect signal. This is due to some phase difference between the raw and extracted backwall reflection signal so that the subtraction cannot make the most effect. Besides, there is another disadvantage of FMC subtraction [22] that the pairs with larger lateral separations, e.g., the first element as transmitter and the last as receiver, will have less averaging effect according to Eq. (8). The effect of backwall reflection subtraction could be worse in those cases.

Another idea that avoids counting backwall reflection signal into the process of HSTFM image reconstruction is to introduce a weight function [22], which is based on the angle between incident and receiving direction of wave. However, this method is invalid when the Snell's law-based wave mode conversion introduced in Sect. 3 is included in this paper. This is simply because the incident wave path is no longer a straight line when the wave mode converts at the backwall.

#### 5 simSUNDT Software

To fully get rid of the influence of backwall reflection signals and to facilitate parametric studies, a UT numerical simulation software, simSUNDT, is utilized. The simSUNDT software consists of Windows®-based pre- and post-processor as well as a mathematic kernel, UTDefect, for the actual modeling and calculation, which has been experimentally validated [23–26] to some extent by comparing with available experimental data. To model the probes and the interaction with defects (scattering), a series of integral transforms and integral equations are employed.

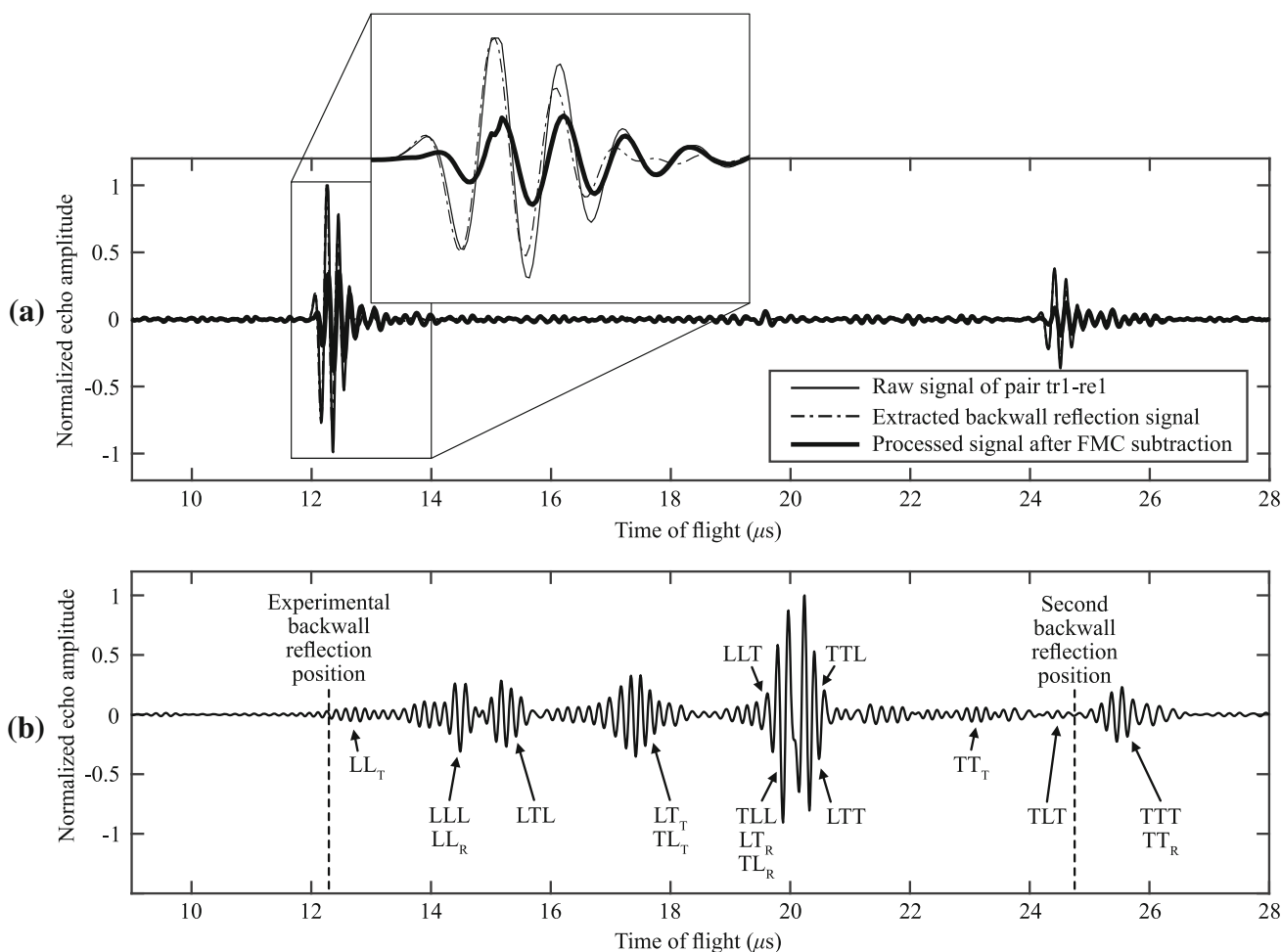


**Fig. 4 a** An example of FMC subtraction result for experimental FMC dataset (pair tr1-re1) of inspection case in Fig. 1 with  $\theta_{rest} \approx 0^\circ$  and  $\theta_{ilt} = 0^\circ$ . Signals shown in the local illustration box clarify different signal plots for the first backwall reflection region. **b** Signal in simulated

FMC dataset (pair tr1-re1) in the same inspection case and time region in (a) with notations of different wave mode components. Subscript “T” and “R” stand for notch tip and root, respectively. Note that the signal amplitudes are all normalized to individual maximum in (a) and (b)

The model is fully three-dimensional, while the simulated component in the software at this stage is limited to be an infinite plate with finite or infinite thickness and bounded by the scanning surface. The probe is modelled as a boundary condition on the surface of an elastic half-space. This surface is traction free except the active part of the contact area beneath the probe. This enables the flexibility of probe simulation regarding its shape, wave type, element size, angles, etc. The receiver in the UT system is modelled by using a widely known and used reciprocity argument [27]. The available defect types are volumetric and crack-like defects, and the methods of solution towards the defect modeling is the T-matrix method [28], where the transition matrix includes all information regarding the defects.

For the considered inspection case in this paper, sim-SUNDT can exclude unnecessary backwall reflections so that there is no such interfering signal [29]. This enables studies

of different physical phenomena caused by the interaction between the ultrasonic wave and the defect characteristics that in an inspection situation normally is disguised by the strong backwall interaction. However, the wave components that potentially have interactions with the notch in question after reflected from the backwall will be included, see Fig. 4b for normalized signal of element pair tr1-re1 in simulated FMC dataset of inspection case in Fig. 1 with  $\theta_{rest} \approx 0^\circ$  and  $\theta_{ilt} = 0^\circ$ , the same as in the experiment case in Fig. 4a. The backwall reflection signals seen in experiment (Fig. 4a) at approximately 12.5 μs and 25 μs are excluded in simulated signal, and other wave mode components that are much smaller in amplitude as to backwall reflection signals can thereby be separated and clearly seen. These wave mode components are indicated with approximate positions in time scale based on estimations. Both direct path mode (indicated by two letters for transmitting and receiving part of the wave



propagation) and half-skip path mode of TFM are included. Note that both notch tip and root have diffracted signals in direct path, which are identified in Fig. 4b by a subscript of “T” for tip diffraction and “R” for root diffraction.

Parametric studies in the next section that exploring the influence of defect features, i.e., notch tilt angle ( $\theta_{ilt}$ ) and relative position between probe center and notch root ( $\theta_{test}$ ), to the capability of defect characterization using TFM images, are performed in this paper based on a series of simulated FMC datasets using simSUNDT. Simulations follow the inspection scenario in Sect. 2 and the used defect type is surface-breaking crack according to the scope and availability of simSUNDT.

## 6 Parametric Studies and Results

In practice, defect characterization using HSTFM is usually conducted by separating the PA probe projection area with defect position, i.e., setting  $\theta_{test} > 30^\circ$  in the inspection scenario in this paper. This is to avoid the interference of the image artifacts induced by backwall reflection signals in experiments, as mentioned in Sect. 4. In this case, a series of FMC datasets with varying  $\theta_{ilt}$  are simulated by simSUNDT and all direct and half-skip path TFM images are reconstructed, with the intention of studying appropriate wave mode sequences that could help with defect characterization. In addition, taking the advantage of simulation software, simSUNDT, that excludes unnecessary backwall reflection signals, another set of studies with  $\theta_{ilt}$  equals  $0^\circ$ ,  $20^\circ$  and  $40^\circ$  under the setting of  $\theta_{test} \approx 0^\circ$  are simulated. It is to illustrate the capability of HSTFM in defect characterization in the case that the probe projection area covers the defect, provided that the backwall reflection signal could be perfectly suppressed.

### 6.1 Case Study 1: Parametric Studies with $\theta_{test} > 30^\circ$

FMC datasets with  $\theta_{ilt} = 0^\circ$  are collected from both experiment and simulation with  $\theta_{test} \approx 36^\circ$  (notch root at  $x \approx 45\text{mm}$  in Fig. 1) to ensure that the potential notch indication in HSTFM image is distinguishable to image artifacts from backwall reflection signals. Then FMC datasets with  $\theta_{test} \approx 36^\circ$  and  $\theta_{ilt} \in [15, 45]^\circ$  (increment of  $5^\circ$ ) are simulated for parametric studies. TFM images are reconstructed for all these cases in all possible direct and half-skip path modes, i.e., 12 wave mode sequences in total. The interpretation of notch tilt angle based on these TFM images are performed through connecting the center of notch tip and root indications in individual TFM image (if possible) and reading the angle towards vertical, presented in Table 1. Note that this process could lead to some minor errors in the outcome due to non-unique choice of the referred reading point.

Figure 5 presents resulting HSTFM images in selected wave mode sequences with normalized image intensity to individual maximum. These certain wave mode sequences are selected so that clear indications are shown and interpretations of notches are possible. Figure 6 presents all direct path TFM images for all these cases with normalized image intensity to individual maximum. Note that the dashed line in all these figures indicates the position of the specimen backwall at 35 mm depth.

The image artifacts from backwall reflection signals are clearly seen in HSTFM images from experimental FMC dataset in Fig. 5a–d under the probe area, i.e., from  $x = 0\text{ mm}$  to  $x = 38.3\text{ mm}$  in Fig. 1. Wave mode sequence TLL in Fig. 5d also shows image artifact at depth 10 to 20 mm above notch indication. Compared to experimental FMC dataset, the corresponding images from the simulated FMC dataset in Fig. 5e–h eliminate the extensive image artifacts and show similar notch indications and artifacts, while the notch indication does not match well in mode TLL in Fig. 5h. In simulation-based parametric studies where  $\theta_{ilt}$  is varied between  $15^\circ$  and  $45^\circ$ , it is seen in Table 1 and Fig. 5i, m, q, u, y, ac and ag that mode LLT preserves the tilt angle and the shape of notch profile until  $25^\circ$ . Above this limit the images show artifacts that make defect characterization impossible. Mode LTT can only show correct tilt angle at  $0^\circ$  and in Fig. 5f, j, n, r, v, z, ad and ah it is confirmed that the shape of notch profile cannot be preserved when  $\theta_{ilt}$  increases from  $0^\circ$ . Mode TTT can only preserve the shape of notch profile until  $15^\circ$  according to Fig. 5g, k, o, s, w, aa, ae and ai and give correct tilt angle until  $20^\circ$  in Table 1. However, mode TLT could mostly preserve the shape of notch profile from  $15^\circ$ , but the interpreted notch tilt angles in Table 1 are always smaller than actual values.

The tip and root indications of the EDM notch from experimental FMC dataset are clearly shown with high intensity in direct path TFM images, especially mode LL as shown in Fig. 6a. Other modes however, i.e., LT, TL and TT in Fig. 6b–d, contain some image artifacts around root indications. Compared to experimental FMC dataset, the corresponding images from simulated FMC dataset in Fig. 6e–h also give clear root indications, while the tip indications are barely visible. This can be explained by weaker diffracted signals from simulated crack tip than real notch tip [30, 31] and will be discussed later. When  $\theta_{ilt}$  increases in parametric studies, the tip indications are more obvious and visible in all direct path modes because more signals from crack tip tend to be received through reflection instead of diffraction. It is then noticed in mode TT when  $\theta_{ilt}$  reaches  $40^\circ$ , as shown in Fig. 6a–f, that the entire crack profile is visible. This is much clearer for all direct path modes when  $\theta_{ilt}$  reaches  $45^\circ$ , see Fig. 6ag–aj.

In brief, it seems that the notch tilt angle can be correctly indicated by mode LLT in HSTFM images between  $15^\circ$  and

**Table 1** Interpretation of notch tilt angle based on all possible wave mode sequences in direct and half-skip path TFM images

	LLL	LLT	LTL	LTT	TTT	TTL	TLT	TLL	LL	LT	TL	TT
T0	0	–	0	0	0	–	–	–	0	–	–	–
T15	–	14	–	–	16	–	9	–	9	16	13	7
T20	–	21	–	–	22	–	13	–	14	20	18	20
T25	–	24	–	19	–	–	18	–	19	24	18	27
T30	–	24	–	23	–	23	25	–	27	28	24	28
T35	–	–	–	28	–	–	29	–	30	32	30	32
T40	–	–	–	34	–	–	32	–	35	37	35	38
T45	–	–	–	41	–	–	37	–	42	43	43	45

The TFM images are reconstructed based on a series of simulated FMC datasets under the inspection scenario in Fig. 1 with  $\theta_{test} \approx 36^\circ$  and varying  $\theta_{ilt}$  (T as in the first column). All values in the table are in unit of  $^\circ$

$25^\circ$ , and after  $25^\circ$  the direct path mode (mode LT and TT) of TFM is more appropriate for identifying and illustrating the notch tilt angle.

When it comes to the weak diffracted signals from crack tip, complementary experiments are performed on two other stainless steel test specimens with mechanical fatigue cracks. Refer to Fig. 1, both these specimens have height ( $h$ ) of 36 mm and the contained fatigue cracks are upright to back-wall ( $\theta_{ilt} = 0^\circ$ ). The respective sizes of the fatigue cracks ( $d$ ) are 7.2 mm and 18 mm. Other inspection parameters remain the same as in Sect. 2. As concerned in the first cases earlier, the experimental FMC datasets are hereby collected with  $\theta_{test} \approx 32^\circ (> 30^\circ)$  to avoid any interference of image artifacts from backwall reflection signals. Resulted TFM images (including both direct path and half-skip path) are shown in Figs. 7 and 8 for fatigue crack sizes of 7.2 mm and 18 mm, respectively. The dashed line in all these figures indicates the position of the specimen backwall at 36 mm depth. Note again that the presented wave mode sequences of HSTFM images are selected so that clear indications are shown and interpretations of fatigue cracks are possible.

From Figs. 6 and 7a–d it again proves that HSTFM can reveal the defect profile, even for real fatigue cracks. In addition, as indicated previously in Fig. 6e–h where the simulated surface-breaking crack has size of 5 mm, the tip indications in direct path TFM images are barely visible for real fatigue crack of size 7.2 mm, see Fig. 7e–h. However, the tip indications in direct path TFM images are clear for fatigue crack of size 18 mm in wave mode sequence of LL, LT and TL, see Fig. 8e–g. This could be explained by the fact that the bigger fatigue crack has its tip closer to the PA probe and the tip diffracted signals can be better captured. Based on these observations and comparison between direct path TFM (mode LL) in Figs. 6a and 7e for experimental data (defects with similar sizes), one can see that the signal behavior of notch and crack tips are dissimilar, and mixing these defect types in practice could be questionable.

## 6.2 Case Study 2: Parametric Studies with $\theta_{test} \approx 0^\circ$

In this study case where the notch root is at  $x \approx 20\text{mm}$  in Fig. 1, FMC datasets with  $\theta_{ilt} = 0^\circ$  are collected from both experiment and simulation. Other simulations with  $\theta_{ilt} = 20^\circ$  and  $\theta_{ilt} = 45^\circ$  are also performed to investigate the characterization capability of HSTFM in this setup. Resulted images are shown in Fig. 9 with normalized image intensity to individual maximum. Only the images of wave mode sequences with clear indications and possible interpretations are shown. The dashed line indicates the position of the specimen backwall at 35 mm depth. HSTFM images from experimental FMC dataset in Fig. 9a–d show expected image artifacts from backwall reflection signals that totally interfere with and overlap the notch indication at  $x \approx 20\text{mm}$ . It is therefore as agreed to be inappropriate for defect characterization in this setup. Corresponding images from simulated FMC dataset in Fig. 9e–h remove the image artifact from backwall reflection signals and can reveal the notch indication to some extent, but other artifacts from the notch signal itself appear even though the intensity is weaker than the notch indication. However, it is observed in Fig. 9h that there is no useful information about the notch itself but only artifacts in TLL wave mode sequence. When  $\theta_{ilt}$  increases, mode LLL can no longer preserve the notch profile as shown in Fig. 9e, i and m, and the defect indication is interfered with image artifacts in other modes, which makes it impossible to characterize the notch. This result could illustrate the fact that characterization of a notch located beneath the probe area using HSTFM is impossible even if the backwall reflection signals and corresponding image artifacts could be entirely eliminated.

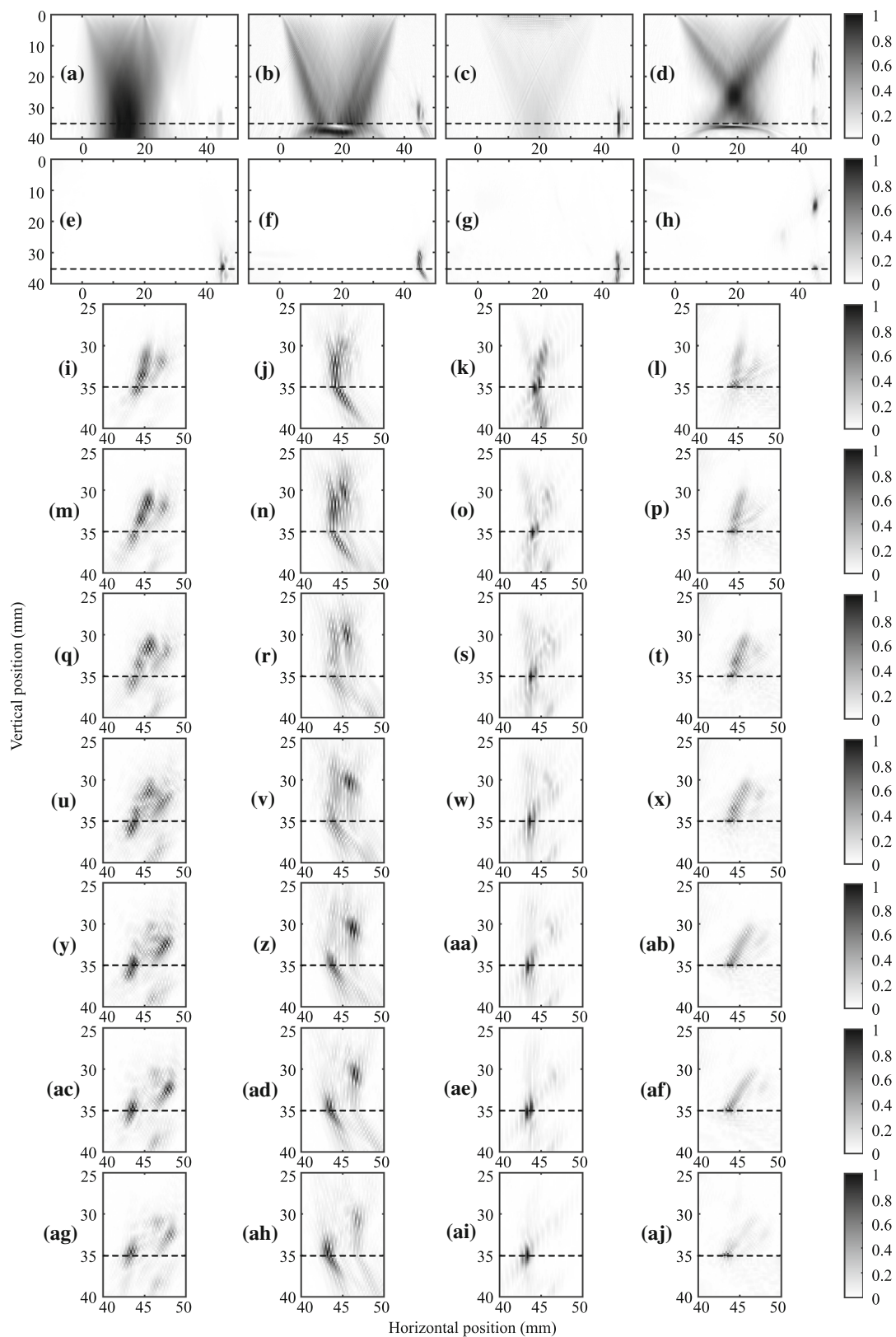
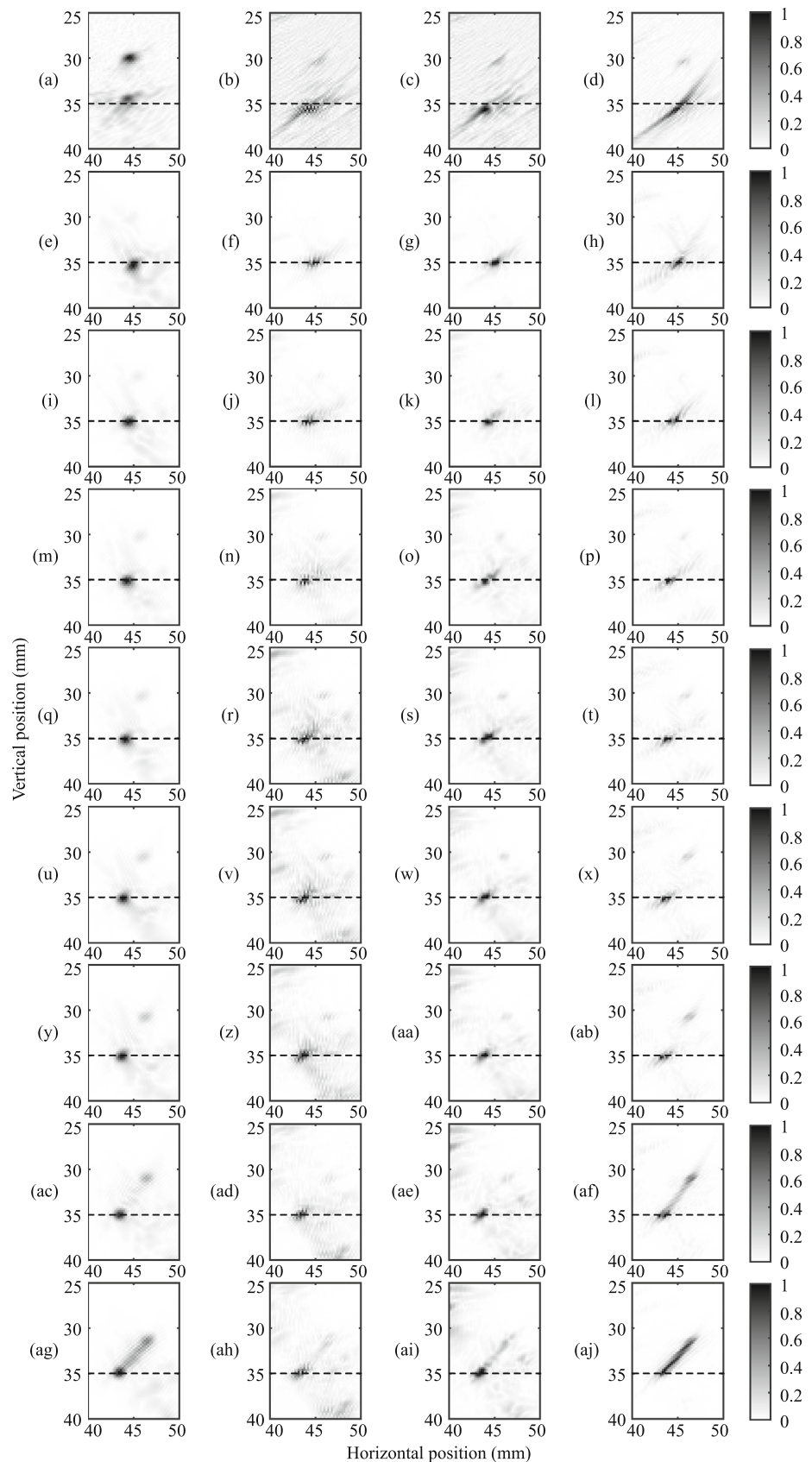


**Fig. 5** Reconstructed HSTFM images in wave mode sequence of **a** LLL, **b** LTT, **c** TTT and **d** TLL for inspection scenario in Fig. 1 with  $\theta_{test} \approx 36^\circ$  based on experimental FMC dataset with  $\theta_{tilt} = 0^\circ$ . The same wave mode sequences are used for simulated FMC dataset in **(e-h)** for the same inspection scenario as in experiment. Wave mode

sequence of **(i, m, q, u, y, ac, ag)** LLT, **(j, n, r, v, z, ad, ah)** LTT, **(k, o, s, w, aa, ae, ai)** TTT and **(l, p, t, x, ab, af, aj)** TLT for simulated FMC dataset with  $\theta_{tilt}$  of **(i-l)**  $15^\circ$ , **(m-p)**  $20^\circ$ , **(q-t)**  $25^\circ$ , **(u-x)**  $30^\circ$ , **(y-ab)**  $35^\circ$ , **(ac-af)**  $40^\circ$  and **(ag-aj)**  $45^\circ$ . The dashed line indicates the position of the specimen backwall at 35 mm depth



**Fig. 6** Reconstructed TFM images in direct path modes in wave mode sequence of **a LL, b LT, c TL and d TT** for inspection scenario in Fig. 1 with  $\theta_{test} \approx 36^\circ$  based on experimental FMC dataset with  $\theta_{tilt} = 0^\circ$ . The same wave mode sequences are used for simulated FMC dataset in **(e–h)** for the same inspection scenario as in experiment. Wave mode sequence of **(i, m, q, u, y, ac, ag) LL, (j, n, r, v, z, ad, ah) LT, (k, o, s, w, aa, ae, ai) TL** and **(l, p, t, x, ab, af, aj) TT** for simulated FMC dataset with  $\theta_{tilt}$  of **(i–l)  $15^\circ$ , (m–p)  $20^\circ$ , (q–t)  $25^\circ$ , (u–x)  $30^\circ$ , (y–ab)  $35^\circ$ , (ac–af)  $40^\circ$  and (ag–aj)  $45^\circ$** . The dashed line indicates the position of the specimen backwall at 35 mm depth



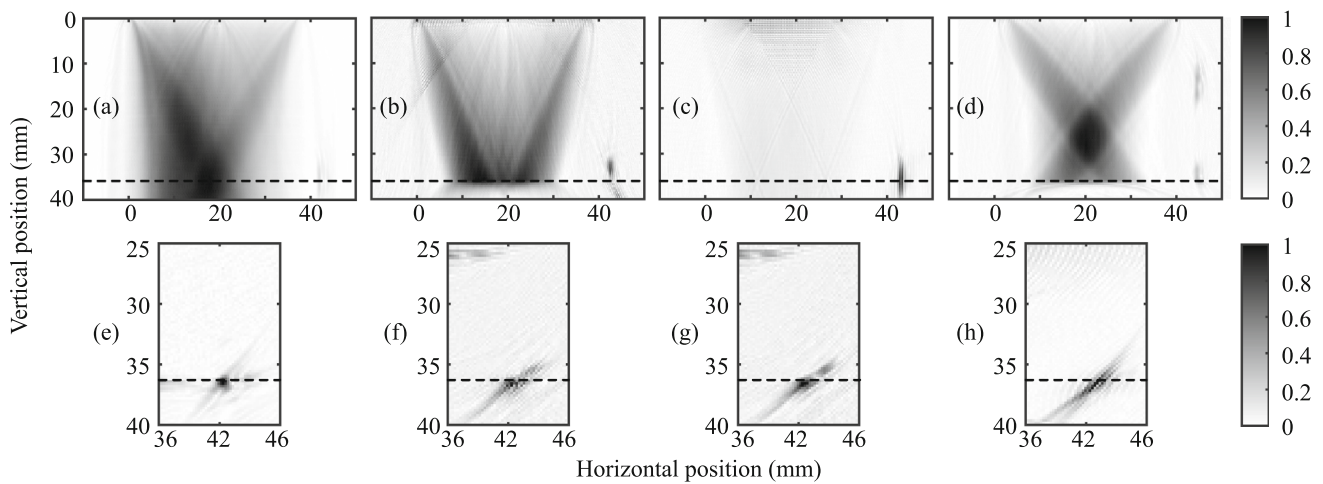


**Fig. 7** Reconstructed HSTFM images in wave mode sequence of **a** LLL, **b** LTT, **c** TTT, **d** TLL and TFM images in direct path modes in wave mode sequence of **e** LL, **f** LT, **g** TL and **h** TT for inspection scenario

in Fig. 1 with upright mechanical fatigue crack of size  $d = 7.2$  mm and  $\theta_{test} > 30^\circ (\approx 32^\circ)$  based on experimental FMC dataset. The dashed line indicates the position of the specimen backwall at 36 mm depth

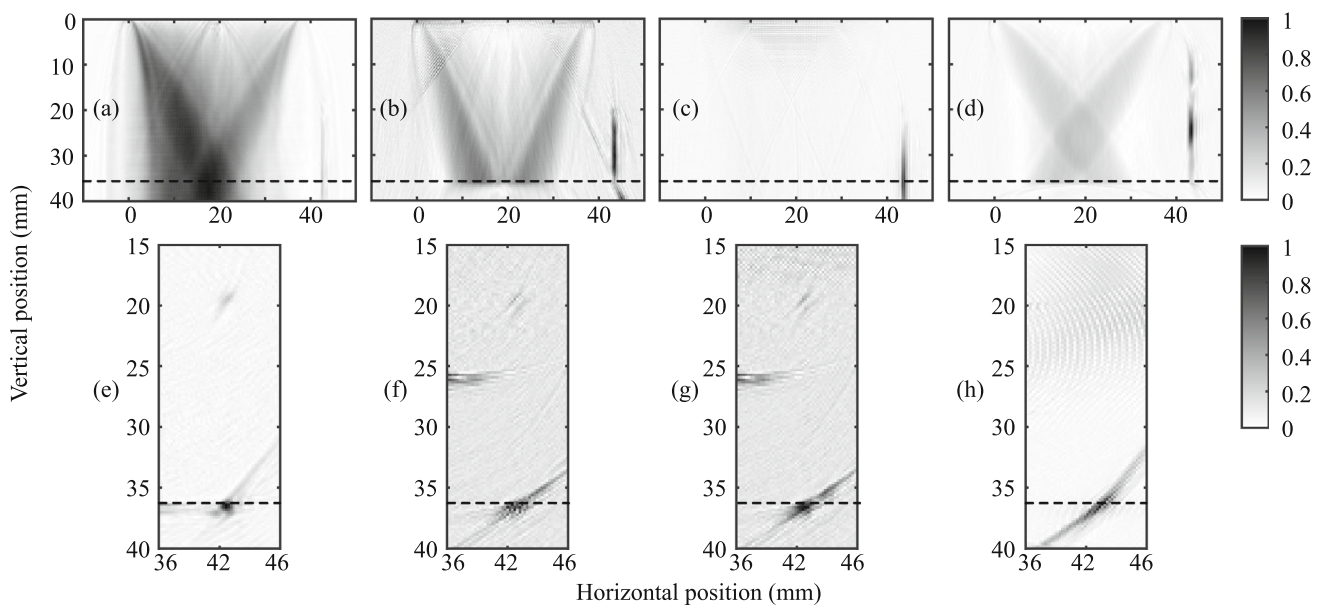


**Fig. 8** Reconstructed HSTFM images in wave mode sequence of **a** LLL, **b** LTT, **c** TTT, **d** TLL and TFM images in direct path modes in wave mode sequence of **e** LL, **f** LT, **g** TL and **h** TT for inspection scenario

in Fig. 1 with upright mechanical fatigue crack of size  $d = 18$  mm and  $\theta_{test} > 30^\circ (\approx 32^\circ)$  based on experimental FMC dataset. The dashed line indicates the position of the specimen backwall at 36 mm depth

## 7 Conclusions

In this paper, an approach that involves Snell's law in accounting propagation time of ultrasound waves in half-skip TFM imaging algorithm is proposed. This intends to address more accurate and reasonable calculation of wave time-of-flight (TOF) when wave mode conversion happens at backwall reflection. Then, some parametric studies are performed with the help of ultrasonic testing simulation software, simSUNDT, to investigate the capability of defect characterization using TFM images. These parametric studies generate a series of FMC datasets, which are based on a

general inspection scenario where the tilt angle and relative position of the considered surface-breaking notch to probe are varied.

In summary, it is noticed and emphasized again from all attempts that the TFM images are sensitive to defect features of concern, and that not all modes are useful to give a clear indication. Different modes and wave mode sequences need to be thoroughly evaluated for a successful interpretation of a certain defect, i.e., with the concept of multi-mode TFM. Seen from the parametric studies, we can see that it is inappropriate to choose a certain wave mode sequence to address all aspects of defect characterization. There is a limit within

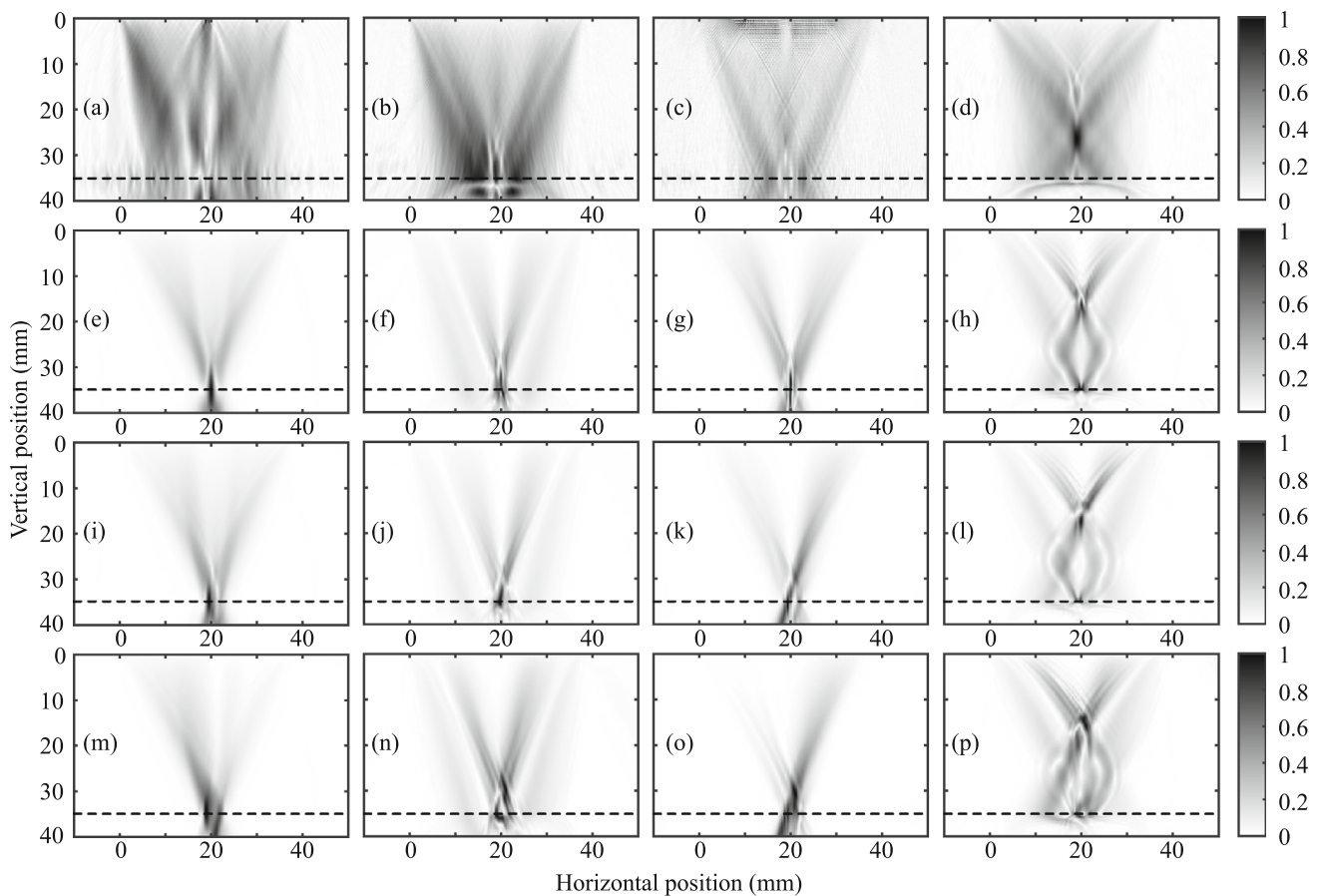


**Fig. 9** Reconstructed HSTFM images in wave mode sequence of **a** LLL, **b** LTT, **c** TTT and **d** TLL for inspection scenario in Fig. 1 with  $\theta_{test} \approx 0^\circ$  based on experimental FMC dataset with  $\theta_{fill} = 0^\circ$ . The same wave mode sequences are used for simulated FMC dataset in **(e–h)** for the

same inspection scenario as in experiment. Wave mode sequence of **(i, m)** LLL, **(j, n)** LTT, **(k, o)** TTT and **(l, p)** TLL for simulated FMC dataset with  $\theta_{fill}$  of **(i–l)**  $20^\circ$  and **(m–p)**  $45^\circ$ . The dashed line indicates the position of the specimen backwall at 35 mm depth

which a mode can work well, but it might not be the case outside this limit. Similarly, some modes only present image artifacts, but it might not be the case if the inspection scenario changes. The parametric studies also show that care must be taken when using HSTFM for defect characterization that the probe projection area should not cover the potential position of the defect. This is because the image artifacts in certain wave mode sequences could come not only from backwall reflection signals, but also from the defect itself.

**Acknowledgements** We appreciate the technical assistance from the Swedish Qualification Centre (SQC) that provides us with the test specimens (ID number: FKA/SQC NR.35, SS36/18 and SS36/7.2 containing EDM notch, fatigue crack of size 18 mm and 7.2 mm, respectively) used in this paper.

**Author Contributions** XL, HW and JEC: have participated in conceptualization and writing—review & editing. HW and JEC: have provided supervision for the work. XL and HW: have provided software, performed formal analysis and collected resources. XL: has done all methodology, validation, investigation, data curation, writing—original draft and visualization. HW: has done all project administration.

**Funding** Open access funding provided by Chalmers University of Technology. Not applicable.

**Data Availability** The data and material are available on request.

## Declarations

**Competing interests** The authors declare that they have no known competing financial interests or personal relationships that could have appeared to influence the work reported in this paper.

**Ethical Approval and Consent to Participate** All authors have consented to participate.

**Consent for Publication** All authors have approved the publication of this manuscript.

**Open Access** This article is licensed under a Creative Commons Attribution 4.0 International License, which permits use, sharing, adaptation, distribution and reproduction in any medium or format, as long as you give appropriate credit to the original author(s) and the source, provide a link to the Creative Commons licence, and indicate if changes were made. The images or other third party material in this article are included in the article's Creative Commons licence,

unless indicated otherwise in a credit line to the material. If material is not included in the article's Creative Commons licence and your intended use is not permitted by statutory regulation or exceeds the permitted use, you will need to obtain permission directly from the copyright holder. To view a copy of this licence, visit <http://creativecommons.org/licenses/by/4.0/>.

## References

- Lopez, A.B., Santos, J., Sousa, J.P., Santos, T.G., Quintino, L.: Phased array ultrasonic inspection of metal additive manufacturing parts. *J. Nondestruct. Eval.* **38**, 62 (2019). <https://doi.org/10.1007/s10921-019-0600-y>
- Geng, C., Shi, W., Liu, Z., Xie, H., He, W.: Nondestructive surface crack detection of laser-repaired components by laser scanning thermography. *Appl. Sci.* **12**, 5665 (2022). <https://doi.org/10.3390/app12115665>
- Ardebili, A., Alaei, M.H.: Non-destructive testing of delamination defects in GFRP patches using step heating thermography. *NDT E Int.* **128**, 102617 (2022). <https://doi.org/10.1016/j.ndteint.2022.102617>
- Brotherhood, C.J., Drinkwater, B.W., Freemantle, R.J.: An ultrasonic wheel-array sensor and its application to aerospace structures. *Insight—Non-Destructive Test. Cond. Monit.* **45**, 729–734 (2003). <https://doi.org/10.1784/insi.45.11.729.52964>
- Chatillon, S., Cattiaux, G., Serre, M., Roy, O.: Ultrasonic non-destructive testing of pieces of complex geometry with a flexible phased array transducer. *Ultrasonics* **38**, 131–134 (2000). [https://doi.org/10.1016/S0041-624X\(99\)00181-X](https://doi.org/10.1016/S0041-624X(99)00181-X)
- Kirk, K.J., McNab, A., Cochram, A., Hall, I., Hayward, G.: Ultrasonic arrays for monitoring cracks in an industrial plant at high temperatures. *IEEE Trans. Ultrason. Ferroelectr. Freq. Contr.* **46**, 311–319 (1999). <https://doi.org/10.1109/58.753019>
- Schmerr, L.W.: *Fundamentals of Ultrasonic Phased Arrays*, vol. 215. Springer, Cham (2015). <https://doi.org/10.1007/978-3-319-07272-2>
- Azar, L., Shi, Y., Wooh, S.C.: Beam focusing behavior of linear phased arrays. *NDT E Int.* **33**, 189–198 (2000). [https://doi.org/10.1016/S0963-8695\(99\)00043-2](https://doi.org/10.1016/S0963-8695(99)00043-2)
- Holmes, C., Drinkwater, B.W., Wilcox, P.D.: Post-processing of the full matrix of ultrasonic transmit–receive array data for non-destructive evaluation. *NDT E Int.* **38**, 701–711 (2005). <https://doi.org/10.1016/j.ndteint.2005.04.002>
- Portzgen, N., Gisolf, D., Blacquièrre, G.: Inverse wave field extrapolation: a different NDI approach to imaging defects. *IEEE Trans. Ultrason. Ferroelectr. Freq. Contr.* **54**, 118–127 (2007). <https://doi.org/10.1109/TUFFC.2007.217>
- Hunter, A.J., Drinkwater, B.W., Wilcox, P.D.: The wavenumber algorithm for full-matrix imaging using an ultrasonic array. *IEEE Trans. Ultrason. Ferroelectr. Freq. Contr.* **55**, 2450–2462 (2008). <https://doi.org/10.1109/TUFFC.952>
- Ying, K.N., Ni, C.Y., Dai, L.N., Yuan, L., Kan, W.W., Shen, Z.H.: Multi-mode laser-ultrasound imaging using Time-domain Synthetic Aperture Focusing Technique (T-SAFT). *Photoacoustics* **27**, 100370 (2022). <https://doi.org/10.1016/j.pacs.2022.100370>
- Zhang, J., Drinkwater, B.W., Wilcox, P.D.: Comparison of ultrasonic array imaging algorithms for nondestructive evaluation. *IEEE Trans. Ultrason. Ferroelectr. Freq. Contr.* **60**, 1732–1745 (2013). <https://doi.org/10.1109/TUFFC.2013.2754>
- Yu P, Gang T.: The use of multi-mode tfm to measure the depth of small surface-break cracks in welds. In: 2017 Far East NDT New Technology & Application Forum (FENDT), IEEE, p. 106–10. <https://doi.org/10.1109/FENDT.2017.8584593> (2017)
- Sy, K., Bredif, P., Iakovleva, E., Roy, O., Lesselier, D.: Development of methods for the analysis of multi-mode TFM images. *J. Phys. Conf. Ser.* **1017**, 012005 (2018). <https://doi.org/10.1088/1742-6596/1017/1/012005>
- Zhang, J., Drinkwater, B.W., Wilcox, P.D., Hunter, A.J.: Defect detection using ultrasonic arrays: the multi-mode total focusing method. *NDT E Int.* **43**, 123–133 (2010). <https://doi.org/10.1016/j.ndteint.2009.10.001>
- Zhang, J., Barber, T., Nixon, A., Wilcox, P.: Investigation into distinguishing between small volumetric and crack-like defects using multi-view total focusing method images. *AIP Conf. Proc.* (2017). <https://doi.org/10.1063/1.4974590>
- Felice, M.V., Velichko, A., Wilcox, P.D.: Accurate depth measurement of small surface-breaking cracks using an ultrasonic array post-processing technique. *NDT E Int.* **68**, 105–112 (2014). <https://doi.org/10.1016/j.ndteint.2014.08.004>
- Felice, M.V., Velichko, A., Wilcox, P.D., Lane, C.J.L.: Depth measurement of small surface-breaking cracks using the half-skip total focusing method. *AIP Conf. Proc.* (2015). <https://doi.org/10.1063/1.4914706>
- Shull, P.J.: *Nondestructive Evaluation*. CRC Press, Boca Raton (2002). <https://doi.org/10.1201/9780203911068>
- Zhang, C., Huthwaite, P., Lowe, M.: The application of the factorization method to the subsurface imaging of surface-breaking cracks. *IEEE Trans. Ultrason. Ferroelectr. Freq. Contr.* **65**, 497–512 (2018). <https://doi.org/10.1109/TUFFC.2018.2793267>
- Zhang, C., Huthwaite, P., Lowe, M.: Eliminating backwall effects in the phased array imaging of near backwall defects. *J. Acoust. Soc. Am.* **144**, 1075–1088 (2018). <https://doi.org/10.1121/1.5051641>
- Jansson, P.A.: Modeling of ultrasonic detection of a rectangular crack. In: *AIP Conference Proceedings*, vol. 509, No. 1, pp. 57–64. <https://doi.org/10.1063/1.1306034> (2000)
- Boström, A., Eriksson, A.S.: Scattering by two penny-shaped cracks with spring boundary conditions. *Proc. R Soc. London Ser. A Math. Phys. Sci.* **443**, 183–201 (1993). <https://doi.org/10.1098/rspa.1993.0139>
- Bövik, P., Boström, A.: A model of ultrasonic nondestructive testing for internal and subsurface cracks. *J. Acoust. Soc. Am.* **102**, 2723–2733 (1997). <https://doi.org/10.1121/1.420326>
- Wirdelius, H.: Experimental validation of the UTDefect simulation software. In: *Proceedings 6th International Conference NDE Relation to Structural Integrity for Nuclear and Pressurized Components*, Budapest, (2007)
- Auld, B.A.: General electromechanical reciprocity relations applied to the calculation of elastic wave scattering coefficients. *Wave Motion* **1**, 3–10 (1979). [https://doi.org/10.1016/0165-2125\(79\)90020-9](https://doi.org/10.1016/0165-2125(79)90020-9)
- Wirdelius, H.: Probe model implementation in the null field approach to crack scattering. *J. Nondestruct. Eval.* **11**, 29–39 (1992). <https://doi.org/10.1007/BF00566015>
- Boström, A.: User guide to UTDefect Version 4: A Computer Program Modelling Ultrasonic Nondestructive Testing of a Defect in an Isotropic or Anisotropic Component. Gothenburg, Sweden (2002)
- Koskinen, A., Haapalainen, J., Virkkunen, I., Kemppainen, M.: Differences in Ultrasonic Indications—Thermal Fatigue Cracks and EDM Notches. In: *18th World Conference Nondestructive Testing*, p. 16–20 (2012)
- Wirdelius, H., Österberg, E.: Study of defect characteristics essential for NDT testing methods ET, UT and RT. (2000)

**Publisher's Note** Springer Nature remains neutral with regard to jurisdictional claims in published maps and institutional affiliations.